ELSEVIER

Contents lists available at ScienceDirect

# Radiation Physics and Chemistry

journal homepage: www.elsevier.com/locate/radphyschem





# Image simulation and realism evaluation for mammography and tomosynthesis based on the detailed breast phantom

Jiahao Wang <sup>a,b</sup>, Yeqi Liu <sup>a,b</sup>, Ankang Hu <sup>a,b</sup>, Shuoyang Wei <sup>a,b</sup>, Tao Wu <sup>c</sup>, Junli Li <sup>a,b</sup>, Rui Qiu <sup>a,b,\*</sup>

- <sup>a</sup> Department of Engineering Physics, Tsinghua University, Beijing, 100084, China
- <sup>b</sup> Key Laboratory of Particle and Radiation Imaging, Tsinghua University, Ministry of Education, Beijing, 100084, China
- <sup>c</sup> Dart Imaging Technology Company, Beijing, 100084, China

#### ARTICLE INFO

Handling Editor: Dr. Chris Chantler

Keywords: Digital mammography Digital breast tomosynthesis Virtual clinical trials Image simulation Breast phantom

#### ABSTRACT

The virtual image system is a key component of virtual clinical trials (VCTs) which can be utilized to evaluate and improve medical imaging devices. The main limitation of VCTs in the Chinese female breast is the lack of detailed structure in the breast model employed in the Chinese specification for testing of quality control in mammography. In this paper, based on Chinese female breast parameters, detailed breast phantoms with different glandularity (fatty, glandular, dense) and compressed breast thicknesses (CBT) (2-7 cm) were generated. Digital mammography (DM) and digital breast tomosynthesis (DBT) projections for these phantoms were simulated with clinical system configuration. Compressed breast volumes were reconstructed through DBT projections with different angles. Power spectrum analysis and fractal dimension measurement were applied for simulated and clinical images. The results show that the average power law exponents and standard deviation (DM, DBT) for clinical and simulated images were (3.26  $\pm$  0.29, 3.33  $\pm$  0.42) and (3.63  $\pm$  0.25, 3.18  $\pm$ 0.36) respectively. The average fractal dimensions and standard deviation (DM, DBT) for clinical and simulated images were (2.36  $\pm$ 0.03, 2.41  $\pm$  0.05) and (2.10  $\pm$  0.01, 2.26  $\pm$  0.06) respectively. We constructed two virtual imaging systems for DM and DBT and obtained the imaging data based on the three-dimensional (3D) detailed breast phantoms. These results indicate that the texture indexes of simulated images are similar to that of the clinical images, and validate that these breast phantoms are suitable for imaging in VCTs requiring realistic anatomy with the Chinese female population. Results also show that the values of power law exponents for clinical and simulated images in DM and DBT are positively correlated with the value of breast glandularity, but the values of fractal dimensions keep steady for different glandularity.

## 1. Introduction

Breast cancer is the most significant threat to women's health in China (Cao et al., 2021). The National Cancer Center of China recommends annual breast cancer screening at least for the female population between the ages of 45 and 70. Digital Mammography (DM) is currently the predominant medical device utilized for breast cancer screening due to its efficiency and cost-effectiveness (Helvie et al., 2014). With the rapid development of technology, Digital Breast Tomosynthesis (DBT), designed to project at multi-angles, has been introduced in the past 20 years (Wu et al., 2003). The characteristic of being able to obtain 'pseudo-3D' information reduces the superposition of fibroglandular inside the breast and improves the visibility of lesions (Tagliafico et al.,

2015). Therefore, in some cases, DM and DBT are combined to diagnose pathologies (Wang et al., 2022).

DM and DBT devices have evolved rapidly in recent years. The complexity and diversity of such devices pose important challenges for application evaluation and design optimization. To assess the diagnostic efficacy versus radiation risks of any new technique, researchers have established clinical trial methods with human subjects. However, conventional clinical trials that request a large number of healthy individuals may take several years. Implementation of these clinical trials appears somewhat impractical and is also limited by various factors such as ethics, cost, and deficiency of ground truth (Abadi et al., 2020).

To solve the problems mentioned above, virtual clinical trials (VCTs) provide an alternative method to effectively evaluate medical imaging

<sup>\*</sup> Corresponding author. Department of Engineering Physics, Tsinghua University, Beijing, 100084, China. E-mail address: qiurui@tsinghua.edu.cn (R. Qiu).

devices by simulating the patient, imaging system, and interpreter (Abadi et al., 2020). It can also be implemented efficiently on a computer and provides investigators with a convenient pattern to make vital questions clear with accurate control and known ground truth. The researchers have employed VCTs in breast X-ray imaging for several applications including(a) verification and improvement of DBT reconstruction methods (Bakic et al., 2010; Zeng et al., 2015), (b) realism evaluation of DM projections and DBT reconstructions (Bliznakova et al., 2010; Elangovan et al., 2017; Graff, 2016; Lau et al., 2012; Li et al., 2009; Mahr et al., 2012; Sturgeon et al., 2017), and (c) glandular dose estimation (Badal et al., 2021; Mettivier et al., 2022b; Sarno et al., 2017a, 2017b; 2018a, 2018b; 2020, 2021; 2022; Wang et al., 2017). At the same time, the risks patients take in clinical applications are minimized. Reviews of the recent development for VCTs in breast X-ray imaging have been published (Barufaldi et al., 2021b; Bliznakova, 2020; Glick and Ikejimba, 2018; Marshall and Bosmans, 2022; Sarno et al., 2023). Breast phantom is a significant part of VCTs in breast X-ray imaging. It can be generated using two approaches: generation from patient data or procedural flow. Patient-derived phantoms present the real shape and glandular distribution of the breast (Caballo et al., 2022; Elangovan et al., 2017; Erickson et al., 2016; Hsu et al., 2013; Li et al., 2009), but are limited by the contrast, spatial resolution, and voxel sizes of the classified images and segmentation methods. (Erickson et al., 2016; Kwan et al., 2007). To address this limitation, procedural phantoms have been developed to simulate the elements of the breast based on anatomical assumptions (Bakic et al., 2002a, 2002b, 2003; Bliznakova et al., 2003, 2010; Bliznakova, 2020; Graff, 2016; Ikejimba et al., 2017; Lau et al., 2012; Pokrajac et al., 2012; Zyganitidis et al., 2007), and to generate larger collections of phantoms with finer details and varying sizes covering a wide spectrum of breast anatomical characteristics. With the development of these phantoms, simulators of the imaging system were required to mimic the medical devices for generating image data. Various radiological image algorithms are proposed to model medical imaging systems. The ray-tracing algorithm was employed to generate projections in the OpenVCT framework developed by Barufaldi et al. (2018). And Badal et al. has released Monte Carlo X-ray imaging simulation software which can be accelerated by Graphics Processing Unit (GPU) (Badal et al., 2021).

To test the performance of VCTs, the texture realism of images produced by simulators needs to be evaluated. Once such instruments are available, various quantitative tasks, including quality control, object detection, and observer performance, could be performed by VCTs efficiently. To better understand the texture realism of clinical mammograms, Burgess (Burgess et al., 2001) discovered that breast structure in a radiographic projection could be characterized by the power spectrum despite nonstationary statistics in mammographic backgrounds. The approach has gained much attention rapidly due to its accuracy and robustness. Furthermore, several studies have shown that breast texture in the mammogram performs as a fractal object (Burgess et al., 2001; Heine and Velthuizen, 2000; Tourassi et al., 2006), and fractal dimension measurement has been investigated as an essential method for mammographic texture assessment (Tourassi et al., 2006). Thus far, power spectrum analysis and fractal dimension measurement have been extensively explored for investigation, comparison, and characterization of breast images (Elangovan et al., 2017; Marinov et al., 2021).

The Chinese specification for testing quality control in mammography or tomosynthesis is mainly based on the imaging of homogeneous breast models (National Health Commission, 2020). Due to the absence of detailed structure, these models cannot be utilized to mimic the texture characteristics with realistic breast anatomy. Our previous studies have developed the fully new breast phantom (Qiu et al., 2017) which contained the detailed structure (e.g. Cooper's ligament, duct tree, ampulla, terminal duct lobular unit, glandular, muscle, adipose, and skin) and have calculated normalized glandular dose coefficients for DM based on the compressed phantoms (National Health Commission, 2021; Wang et al., 2017). The breast phantom exhibits acceptable

texture features in breast imaging due to a series of characteristics, such as detailed structures, randomly irregular boundaries of the subcutaneous adipose and fibroglandular regions, and the random sampling distribution of adipose lobules. In this paper, we constructed two imaging systems for DM and DBT respectively, and obtained the simulated images based on the detailed breast phantom. To evaluate the texture realism of simulated images, power spectrum analysis, and fractal dimension measurement were employed for quantitative assessment. These methods were also employed on the clinical datasets to compare the texture properties. Concerning this investigative step, our final goal was to develop software that could generate the breast phantom with good performance in dosimetry and imaging and to investigate the optimal exposure parameters for individual patients during the breast screening which could balance the radiation dose and image quality.

## 2. Materials and methods

## 2.1. Detailed breast phantoms

Breast phantoms were generated by the simulation chain described by Wang (Wang et al., 2017) et al. Research showed that the volumetric breast density (VBD) of Chinese women is mainly concentrated in 17.3%  $\pm 8.2\%$  (Wang et al., 2017). Breast phantoms of 25%, 50%, and 75% glandularity were constructed to represent fatty, glandular, and dense breasts in this work. The corresponding VBD of these phantoms were 8.2%,16.6%, and 25.4%. The glandularity and VBD are two physical quantities to indicate the amount of glandular tissue using mass and volume percentage. They are calculated by the following equations, respectively.

glandularity = 
$$m_g/M_{fg} \times 100\%$$

$$VBD = V_g / V_{br} \times 100\% \tag{1}$$

Where  $m_g$  is the mass of glandular tissue,  $M_{fg}$  is the whole mass of the fibroglandular region,  $V_g$  is the volume of glandular tissue,  $V_{br}$  is the volume of the breast model. Through the deformations for the vertical slices, detailed breast phantoms with each glandularity were compressed to 2 cm, 3 cm, 4 cm, 5 cm, 6 cm, and 7 cm in the craniocaudal (CC) view. One breast phantom sample is shown in Fig. 1. Overall, 18 compressed breast phantoms were generated for image acquisition in DM and DBT.

## 2.2. Image acquisition simulation

#### 2.2.1. X-ray spectrum

The spectra produced by the target of the X-ray tube in medical equipment are not monoenergetic. Polyenergetic X-ray spectra acquired from the spectral model of Boone (Boone et al., 1997) were simulated during the image acquisition process. The X-ray spectra were simulated for DM using tungsten (W) targets and silver (Ag) or rhodium (Rh) filtering materials. While the X-ray spectra were simulated for DBT using W targets with aluminum (Al) filtering materials. For breast phantoms with different CBTs, we adopted the suggestions about the choice of target/filter combination and tube voltage in ref. (Massera and Tomal, 2021).

## 2.2.2. Tissue composition

Table 1 lists the density and element composition of each breast tissue which was acquired from ICRU-Report 46, Woodard, and White (Woodard and White, 1986). Values for Cooper's ligament tissue were not specifically provided by ICRU, so the density and element composition of Cooper's ligament tissue was substituted by these of muscular fibrous tissue (Ma et al., 2009).

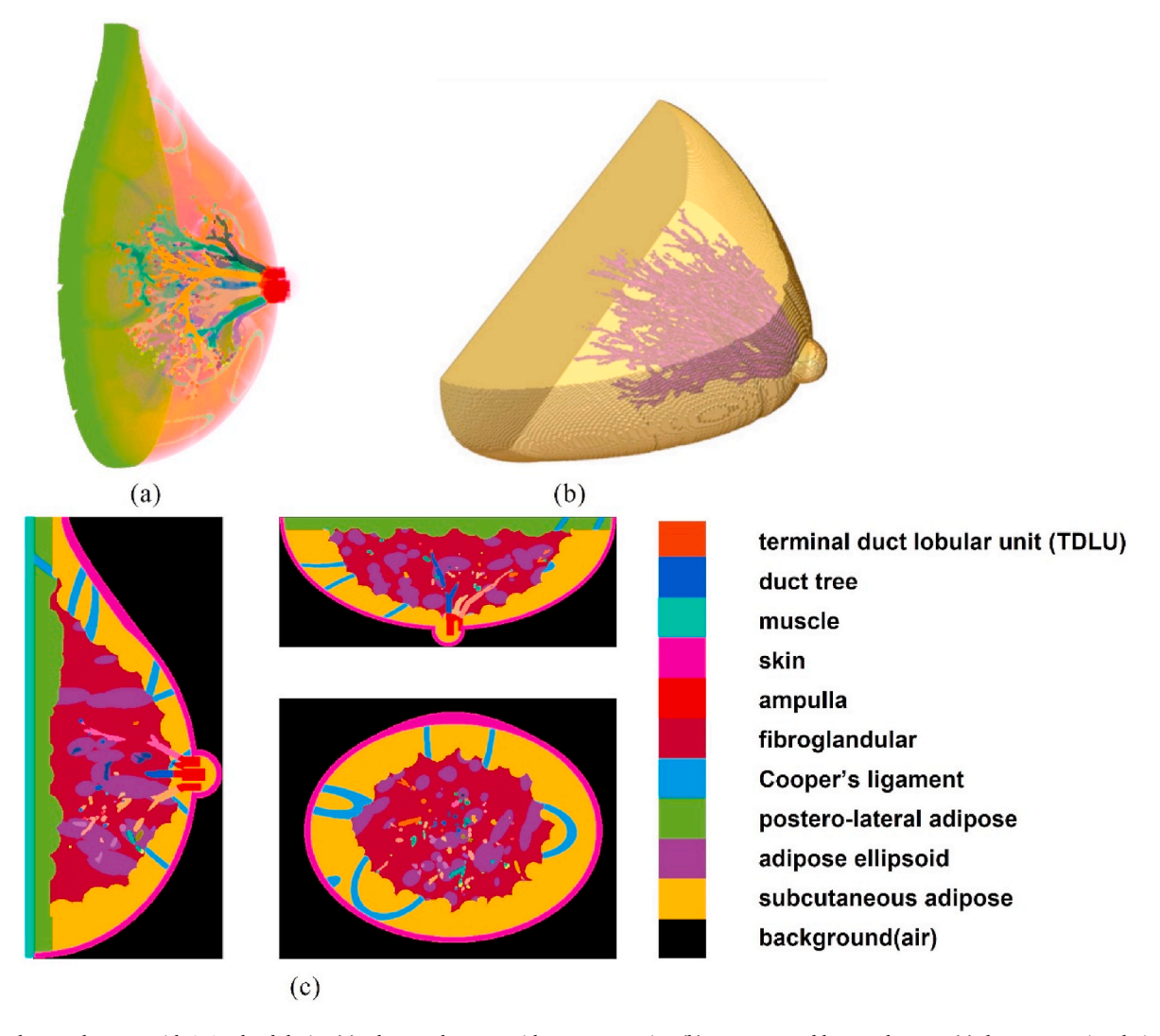


Fig. 1. One breast phantom with 25% glandularity (a) a breast phantom without compression (b) a compressed breast phantom (c) the cross-sectional views of the uncompressed breast phantom from coronal (left), sagittal (right-up), and axial (right-down) directions.

**Table 1**Density and Element composition of each breast tissue.

Tissue	Density (g/m³)	Element c	Element composition (%)							
		Н	С	N	0	Na	P	S	Cl	K
Skin	1.09	10.0	20.4	4.2	64.5	0.2	0.1	0.2	0.3	0.1
Adipose	0.95	11.4	59.8	0.7	27.8	0.1	0.1	0.1	0.1	_
Glandular	1.02	10.6	33.2	3.0	52.7	0.1	0.1	0.2	0.1	-
Cooper's ligament	1.05	10.2	14.3	3.4	71.0	0.1	0.2	0.3	0.1	0.4

## 2.2.3. Equivalent mass attenuation coefficients for breast tissues

In terms of polyenergetic spectra, the number of photons that are attenuated by the compound matter is calculated by:

$$I = I_0 \bullet \sum_{E=E_{min}}^{E=E_{max}} f(E) e^{-\sum_{i=1}^{n} \mu_{mi}(E)x_{mi}} \Delta E$$
 (2)

Where  $I_0$  and I are the photon intensity for emission and detection (passed through the object) respectively,  $\mu_{mi}$ ,  $x_{mi}$  are the mass attenuation coefficient and mass thickness of the  $i^{th}$  element respectively, note that the mass thickness is defined as the mass per unit area, and is obtained by multiplying the thickness t by the density  $\rho$ , i.e.,  $x_m = \rho t$ , n is the number of elements in the object, f(E) is the distribution function of

the photon spectrum,  $\Delta E$  is the energy interval in the discrete photon spectrum.

In terms of monoenergetic spectra, the mass attenuation coefficient of the compound  $\mu_c$  is defined as:

$$\mu_c = \sum_{i=1}^n \mu_{mi} c_i \tag{3}$$

Where  $c_i$  is the weight fraction of the  $i^{th}$  element in the compound. Substitute equation (3) into equation (2), and get the mass attenuation coefficient of the compound for polyenergetic spectra (Gorshkov, 2017)

$$\mu_{c} = \lim_{x_{m} \to 0} - \frac{1}{x_{m}} \sum_{E = E_{min}}^{E = E_{max}} f(E) e^{-\mu_{c}(E)x_{m}} \Delta E = \sum_{E = E_{min}}^{E = E_{max}} \mu_{c}(E) f(E) \Delta E = \overline{\mu_{c}(E)}$$

We adopted the mass attenuation coefficient values of each element from the national institute of Standards and technology (NIST) (Hubbell and Seltzer, 2004) and employed the cubic spline method for interpolation to acquire the mass attenuation coefficient of each energy value.

#### 2.2.4. Image simulation

DM and DBT projections of the breast phantoms were simulated using the open-source MATLAB toolbox, named LAVI DBT-Reconstruction toolbox, which can be accelerated by parallel computation methods. This code was chosen for the successful validation with the virtual Shepp-Logan phantom in Ref. (Vimieiro et al., 2018).

To simulate the radiological projections, the Hologic Selenia Dimensions 3D system (Hologic, MA, USA) geometries were constructed for both DM and DBT. As displayed in Fig. 2, the X-ray tube rotates around the rotation center in the imaging geometry of DBT, while the X-ray tube keeps static at  $0^{\circ}$  in the imaging geometry of DM. The geometrical parameters used in the image simulation are presented in Table 2.

The projection of a breast phantom was drawn using the ray tracing algorithm. Each pixel value of the projected image was calculated by the radiological path of the ray within the detector. The radiological path can be written as

$$d = \sum_{i} \sum_{j} \sum_{k} \mu_{c}(i, j, k) l(i, j, k)$$
 (5)

Where i,j, and k are the coordinates of each voxel in the 3D phantom matrix,  $\mu_c(i,j,k)$  is the equivalent mass attenuation coefficient of a particular voxel and l(i,j,k) is the ray track length contained by that voxel. The detector model was assumed to be ideal and scatter radiation was not included in the projections.

According to the conclusion in Ref (Vancamberg et al., 2015)., the power spectrum of a reconstructed volume was influenced by the reconstruction algorithm. Therefore, the algorithm adapted to simulated images should be consistent with that of clinical images. The filtered back-projection algorithm (FBP) was utilized to solve the inverse reconstruction problem based on the simulated DBT projections.

## 2.3. Objective evaluation of image texture

To evaluate the texture realism of simulated images, we selected clinical images from public medical datasets for comparison. Clinical

**Table 2**Geometry parameters for DM and DBT.

X-ray modality	DBT	DM
Target material	W	W
Filter material and thickness	0.7 mm Al	0.05 mm Rh/Ag
Angle range (°)	[-15°,15°]	_
Number of Projections (#)	15	1
Detector		
Detector Element Size (mm)	0.14	0.07
Detector Size (mm)	$286.72\times232.96$	$286.72\times232.96$
Distance source to the detector (DSD) (mm)	700	700
Distance detector to rotation (DDR) (mm)	0	0
Distance of the Air Gap (DAG) (mm)	25	25

mammograms were chosen from the Mammographic Image Analysis Society Digital Mammogram Database (MIAS) (Suckling et al., 2015). The images of this dataset containing obvious lesions were excluded. The remaining mammograms contained three types of glandularity: fatty, glandular, and dense, with 66, 130, and 142 images in each category respectively. For each image contained in the dataset, glandularity classifications had been determined by experienced radiologists and were included in the readme file. Clinical DBT reconstructed volumes were obtained from the Breast Cancer Screening dataset (BCS) (Buda et al., 2021). We took the analysis for the mid-plane of each reconstructed volume for which an experienced radiologist has determined the glandularity classification. For the fatty, glandular, and dense categories, 70, 140, and 140 images were selected respectively. Following the approach of Barufaldi (Barufaldi et al., 2021a), we employed the OpenBreast toolkit (Pertuz et al., 2019) to locate a region of uniform thickness excluding pectoralis muscle, background, and a 10 mm boundary. This region was defined by a binary mask. These processes were also implemented on the simulated images.

# 2.3.1. Power spectrum analysis

For the comparison of texture realism between clinical and simulated images, power spectrum analysis was employed due to its robustness. The texture properties in clinical breast images could be indicated by the power law exponent in Equation (6)

$$PS_{1D}(f) = \alpha/f^{\beta} \tag{6}$$

Where  $\alpha$  is the magnitude of one-dimensional power spectrum ( $PS_{1D}$ ),  $\beta$  is the power law exponent that can reflect the breast texture complexity, and f is the spatial frequency. The meaning and calculation procedure of  $PS_{1D}$  are described in detail below. Unprocessed mammograms and the

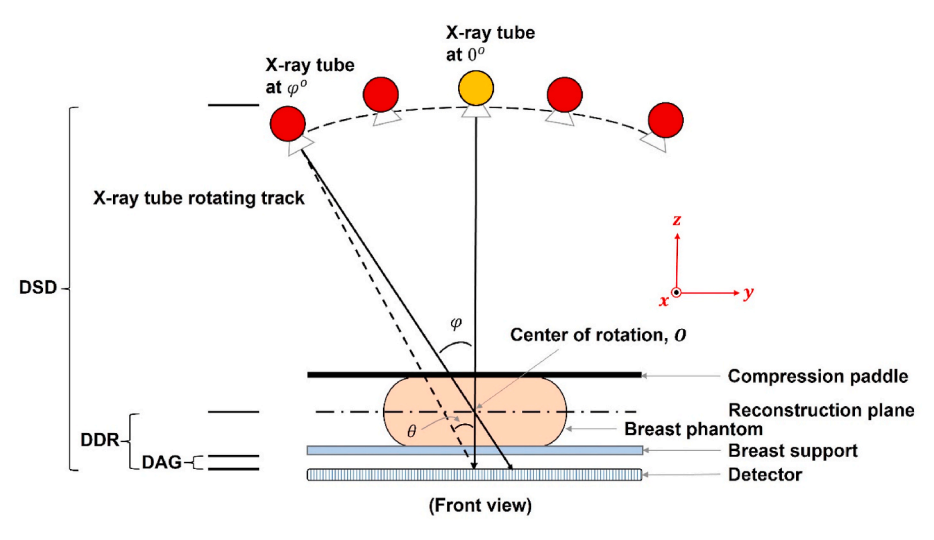


Fig. 2. Imaging geometry for the simulation of DBT and DM with the breast phantom.

mid-plane of reconstructed DBT volumes were analyzed by this method.

The steps of the power spectrum analysis procedure are explained with an example image in Fig. 3. The first step is the determination of the region of interest (ROI) with a suitable position and size. A size of 512  $\times$ 512 pixels (35.84 mm on each side) of the ROI was cropped from the example image (Barufaldi et al., 2021a). To ensure that valid pixel values can be extracted, the center of the ROI was located by determining the mass-center of the binary mask for the example image. The second step is pre-processing of the ROI. The ROI was normalized by the average pixel value and then was processed by a radial Hanning window for reducing the frequency leakage during the fast Fourier transform. The third step is the calculation of the power law exponent. we obtained the two-dimensional (2D) power spectrum of the ROI after the fast Fourier transform. By averaging along the radial direction of the 2D power spectrum,  $PS_{1D}$  was obtained. To limit the effect of detector noise and spatial information which is not associated with breast texture, the range of 0.2-1.0 mm<sup>-1</sup> for spatial frequency was selected (Barufaldi et al., 2021b; Elangovan et al., 2017). For simulated images, we also select the same spatial frequency range for the calculation of  $\beta$  values. Finally, the plot of  $\log_{10}(PS_{1D})$  versus  $\log_{10}(f)$  during this range was performed by the linear fitting method. The absolute slope value obtained from the fitted line is the power law exponent  $\beta$ . To determine the  $\beta$  value that represents the breast image more accurately, we moved the ROI along the four directions (up, down, right, and left) with the maximum movement (does not exceed mask area) and took the average value. The relative differences  $\Delta_{\beta}$  between the simulated and clinical images can be calculated by:

$$\Delta_{\beta} = (\beta_{simulated} - \beta_{clinical}) / \beta_{clinical} \times 100\%$$
(7)

#### 2.3.2. Fractal dimension measurement

Fractal dimension (FD) is a generic term that is related to the texture complexity of objects and was calculated by the published methods (Bliznakova et al., 2010; Elangovan et al., 2017). For an image surface, we can measure it by covering it with a cube of side length  $\varepsilon$ . As the side length  $\varepsilon$  of the cube increases, the covered cube blocks also change. The exposed surface area,  $A(\varepsilon)$ , of the covered cube blocks and FD of the image surface are related by the following formula (8)

$$A(\varepsilon) = \lambda \varepsilon^{2-FD} \tag{8}$$

where  $\lambda$  is a scaling constant. The area  $A(\varepsilon)$  was calculated by the following equation (9).

$$A(\varepsilon) = \sum_{x,y} \varepsilon^2 + \sum_{x,y} \varepsilon |I(x,y) - I(x+1,y)| + \sum_{x,y} \varepsilon |I(x,y) - I(x,y+1)|$$
 (9)

Where I(x,y) is the amounts of cubes with a side length  $2^i$ , for  $i=0,1,2,\ldots 7$ , in the specific position (x,y). Finally, the plot of  $\log_{10}(A(\varepsilon))$  versus  $\log_{10}(\varepsilon)$  was performed by the linear fitting method. The FD can be

determined by the slope value which is obtained from the fitted line. In order to determine the FD value that represents the breast image more accurately, we adapted the same method with power spectrum analysis to move the ROI and take the average value. The relative differences  $\Delta_{FD}$  between the simulated and clinical images can be calculated by:

$$\Delta_{FD} = (FD_{simulated} - FD_{clinical}) / FD_{clinical} \times 100\%$$
(10)

## 2.4. Implementation

All analyses were performed using MATLAB scripts (MATLAB R2021b; MathWorks). Moreover, to accelerate the FBP reconstruction process, the code was parallelized on a Linux node with 132 GB RAM and 28 slave processors of the high-performance computing platform at Tsinghua University. Reconstructed phantoms with each CBT and glandularity were generated using parallel computing code.

#### 3. Results

## 3.1. Imaging simulation

Based on the geometrical parameters in Table 2, the 3D imaging system geometries were replicated for both DM and DBT. Fig. 4 shows the 3D imaging geometry using the LAVI toolbox. Fig. 5 shows the DM projection and the DBT reconstructed mid-plane image of the breast phantom with 50% of glandularity and 4 cm CBT, respectively. These pictures were performed with a simple contrast stretch to turn into brighter.

#### 3.2. Power spectrum analysis

The power law exponent  $\beta$  was calculated for each clinical and simulated ROI. Fig. 6 presents a comparison of the calculated metrics between simulated and clinical images for both DM and DBT. The linear trends of the power law exponent were compared in Fig. 6a–d (the second column).

The MIAS and BCS dataset was divided into three categories based on glandularity ranks. Table 3 lists the power law exponents for clinical and simulated images at different glandularity; errors are denoted as 1 standard deviation (SD) of the average value.

For each image, the correlation coefficient for the fitted line between the  $\log_{10}PS_{1D}(f)$  and the  $\log_{10}f$  was calculated. In the case of simulated images, the average correlation coefficients and standard deviation are  $r=0.98\pm0.01$  and  $r=0.98\pm0.01$  for DM and DBT, respectively, while for ROIs extracted from clinical images taken from MIAS and BCS, the coefficients and standard deviation are  $r=0.99\pm0.01$  and  $r=0.99\pm0.01$ , respectively. The correlation coefficients for all fitted lines are higher than 0.95. A good linear relationship between the  $\log_{10}PS_{1D}(f)$  versus  $\log_{10}f$  during the specific range is observed. The

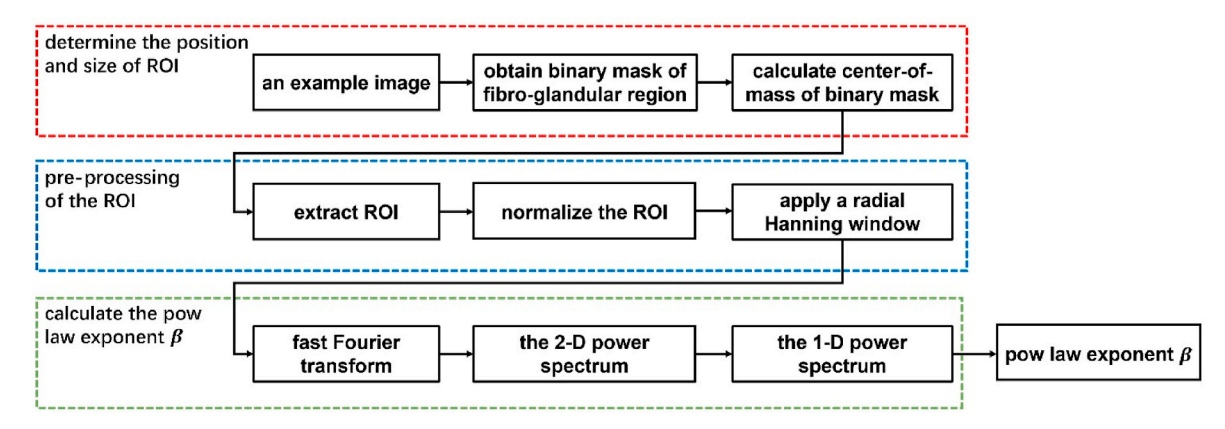


**Fig. 3.** The steps to obtain the pow law exponent  $\beta$  during the analysis procedure.

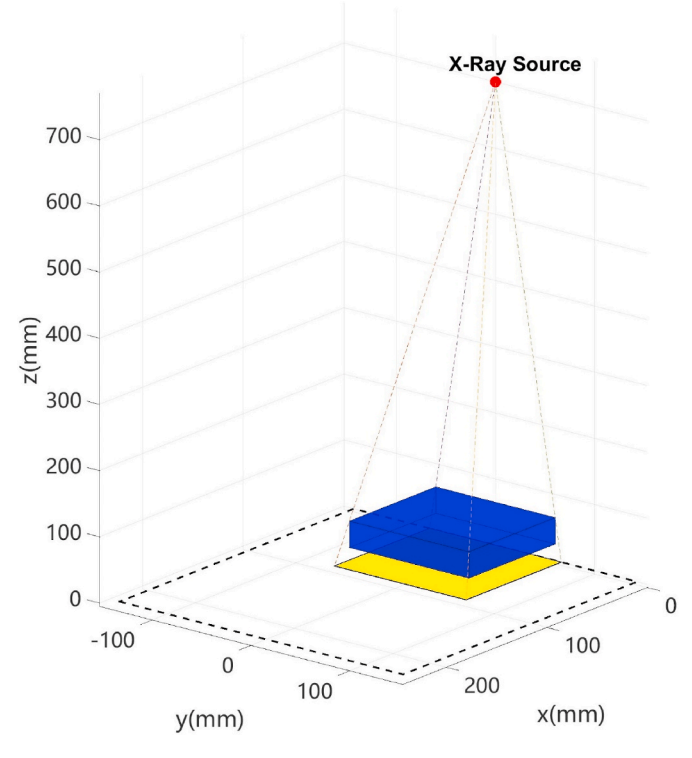


**Fig. 4.** 3D imaging geometry based on Hologic imaging parameters. The red dot is the X-ray source. The dark blue cube is a 3D voxel matrix of the breast phantom. the dashed rectangle in the x-y plane represents the detector plane, where the yellow part is the projection area.

relative differences  $\Delta_{\beta}$  between the simulated and clinical images for DM and DBT are 11.35% and -4.50%, respectively.

#### 3.3. Fractal dimension measurement

The fractal dimensions were calculated for each simulated and real image. The linear trends for fractal dimensions which were calculated by simulated and clinical images were compared in Fig. 6a–d (the third

column). Table 4 lists the fractal dimension, showing a similar result between the simulated and clinical images.

For each image, the correlation coefficient for the fitted line between the  $\log_{10}A(\varepsilon)$  and the  $\log_{10}(\varepsilon)$  was calculated. In the case of simulated images, the average correlation coefficients and standard deviation are  $r=0.96\pm0.02$  and  $r=0.97\pm0.01$  for DM and DBT, respectively, while for ROIs extracted from clinical images taken from MIAS and BCS, the coefficients and standard deviation correspond to  $r=0.95\pm0.01$  and  $r=0.99\pm0.01$ , respectively. The correlation coefficients for all fitted lines are higher than 0.90. A good linear relationship between the  $\log_{10}A(\varepsilon)$  and the  $\log_{10}(\varepsilon)$  is observed. The relative differences  $\Delta_{FD}$  between the simulated and clinical images for DM and DBT are -10.88% and -6.06%, respectively.

#### 4. Discussion

Several recent studies have shown that VCTs are essential for the evaluation and improvement of medical devices (Abadi et al., 2020; Barufaldi et al., 2021a; Elangovan et al., 2017). These studies have demonstrated that VCTs can provide detailed and accurate information about the performance of medical devices, which can be used to identify areas for improvement and optimize device design. The initial aim of this study was to construct virtual image systems for both DM and DBT and evaluate image texture realism. Based on the detailed breast phantoms, we obtained the projections for mammography and the reconstructed breast volumes for DBT, and evaluate the texture realism of these simulated images. According to the results displayed in Tables 3 and 4, the simulated images have a close resemblance to the clinical images in terms of texture indexes. Our results were consistent with some of the previous literature. Barufaldi et al. achieved a lower discrepancy between simulated and clinical DM images, from 14.15% to 11.25%, by applying Perlin noise to the breast phantom (Barufaldi et al., 2021b). The  $\beta$  values of simulated DM images in Bochud et al.'s research and clinical DM images in Cockmartin et al.'s research were (3.4, 4.0) and 3.57 respectively (Bochud et al., 1999; Cockmartin et al., 2013). However, some other literature results differed from ours, such as Graff et al.'s model that produced  $\beta$  values of (2.72,2.95) (Graff, 2016).

But there are still discrepancies in the results between the clinical and simulated images. The mean  $\beta$  of simulated mammograms is a little higher than that of clinical images acquired from MIAS, while the mean

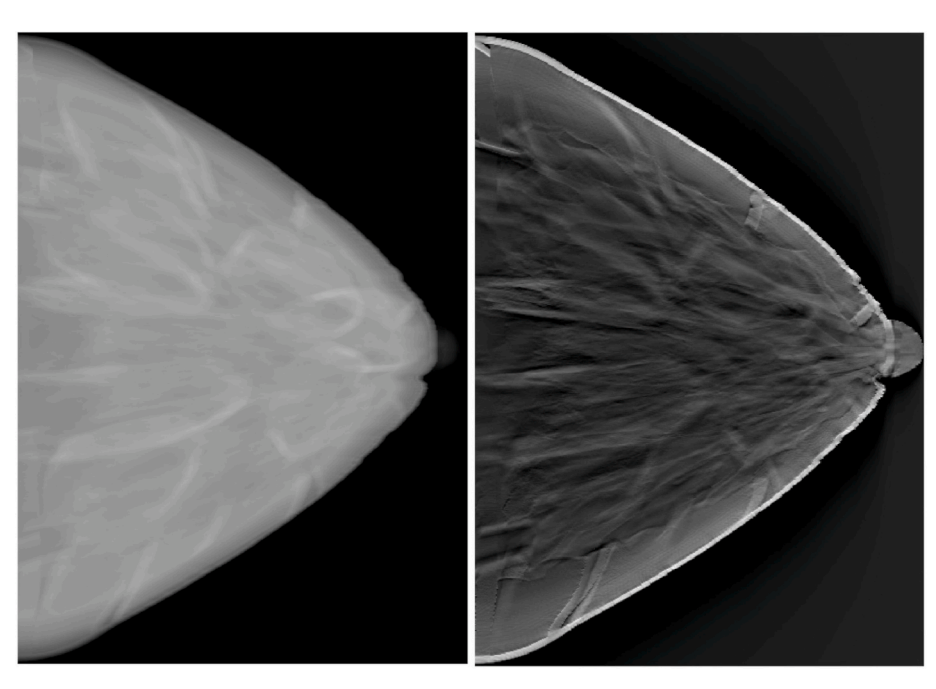


Fig. 5. The DM projection and the DBT reconstructed mid-plane image of the breast phantom with 50% of glandularity and 4 cm CBT.

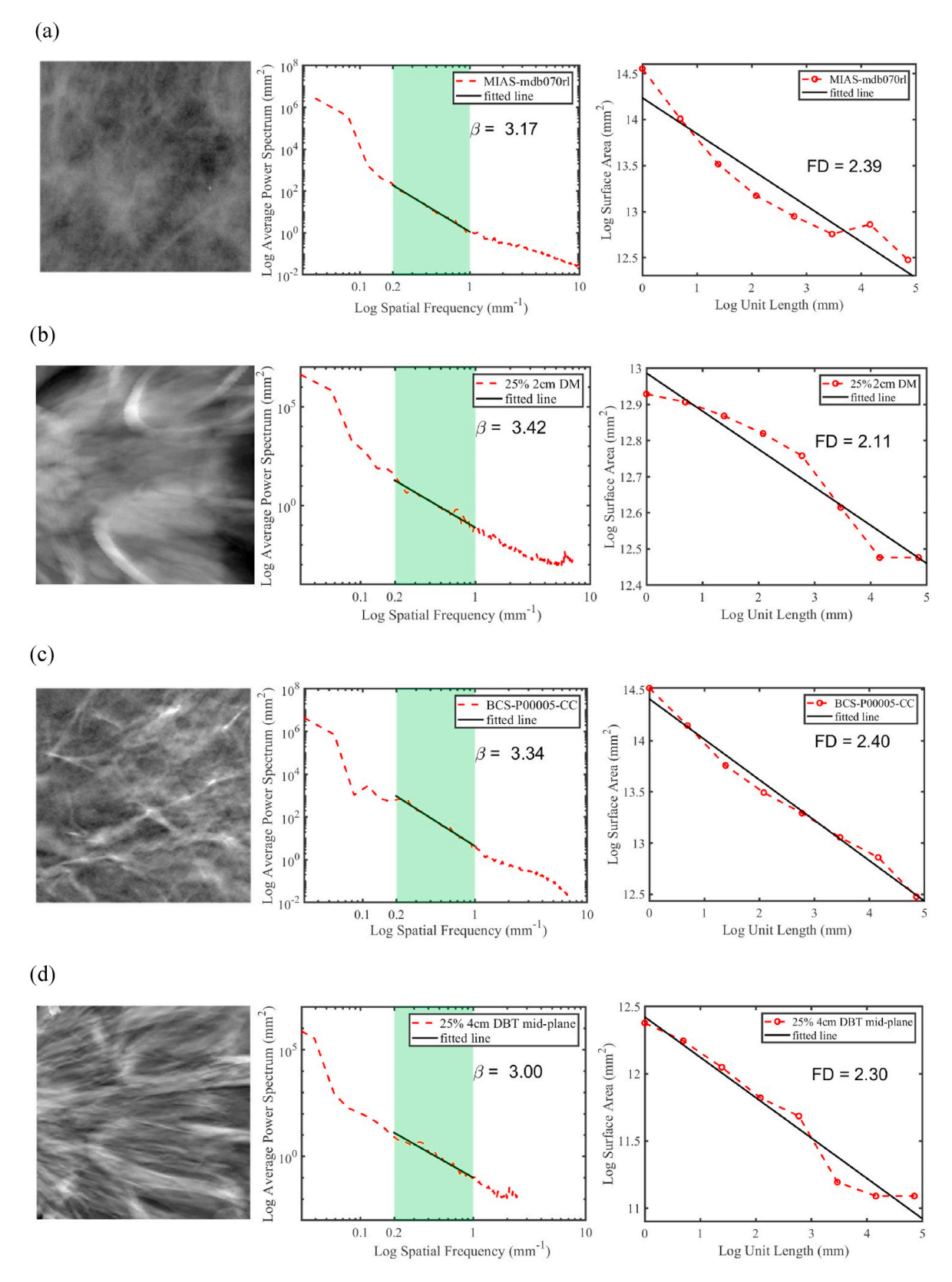


Fig. 6. ROIs for clinical and simulated images, and their corresponding calculated metrics for power spectrum analysis and fractal dimension measurement. (a) a clinical mammogram taken from MIAS; (b) the mammography projection for the breast phantom with 25% glandularity and 2 cm CBT; (c) the mid-plane of clinical breast tomosynthesis reconstructed volume for the breast phantom with 25% glandularity and 4 cm CBT.

**Table 3** Results of power law exponents  $\beta$  of clinical and simulated images with different glandularity.

Glandularity	DM		DBT		
	MIAS $\beta \pm SD$	Breast phantom $\beta \pm SD$	BCS $\beta \pm SD$	Breast phantom $\beta \pm SD$	
Fatty	$3.05 \pm 0.30$	$3.51 \pm 0.27$	$3.15 \pm 0.36$	$3.04 \pm 0.39$	
Glandular	$3.28 \pm 0.26$	$3.62 \pm 0.26$	$3.39 \pm 0.35$	$3.22 \pm 0.36$	
Dense	$3.42 \pm 0.23$	$3.77 \pm 0.22$	$3.50 \pm 0.40$	$3.29 \pm 0.35$	
All	$3.26 \pm 0.29$	$3.63 \pm 0.25$	$3.33 \pm 0.42$	$3.18 \pm 0.36$	

**Table 4**Fractal dimensions of real and simulated images.

Glandularity	DM		DBT		
	MIAS $FD\pm$ $SD$	Breast phantom $FD \pm SD$	BCS FD ± SD	Breast phantom $FD \pm SD$	
Fatty Glandular Dense All	$2.39 \pm 0.03$ $2.36 \pm 0.03$ $2.33 \pm 0.03$ $2.36 \pm 0.03$	$2.10 \pm 0.01$ $2.10 \pm 0.01$ $2.11 \pm 0.01$ $2.10 \pm 0.01$	$2.43 \pm 0.05$ $2.42 \pm 0.04$ $2.38 \pm 0.06$ $2.41 \pm 0.05$	$2.27 \pm 0.07$ $2.27 \pm 0.06$ $2.25 \pm 0.05$ $2.26 \pm 0.06$	

FD of simulated images is a little lower than that of clinical images. There are several possible explanations for these results. Firstly, scattered radiation and detector characteristics in clinical medical devices have a positive effect on the high-frequency signal (Badal et al., 2021). But the ray tracing algorithm employed in the imaging process ignores these noises. The decrease in the high-frequency signal will cause  $\beta$  to rise slightly. Another reason is the absence of the high-frequency signal texture structure within breast phantoms. The microstructure within the breast, including adipose globules and Cooper's ligament, is represented by smooth ellipsoid surfaces. An experienced radiologist pointed out that the obvious Cooper's ligament in the simulated images will reduce the texture realism. Except for these reasons, the simulated images of DM were unprocessed, but the clinical images dataset were all "for presentation". This difference may make discrepancies in the calculation metric results.

What stands out in Table 3 is the increase of power law parameter  $\beta$  with glandularity for clinical and simulated images. The result is consistent with Ref (Mainprize et al., 2012). These relationships can be explained by the texture complexity of fibroglandular. As glandularity increases, fibroglandular tissue appears to congregate and flatten out, leading to a decrease in high-frequency signal and an increase in  $\beta$  value. Interestingly, power law parameter  $\beta$  of simulated mammograms with lower CBTs and glandularity is close to the mean value of clinical dataset. In terms of the fractal dimensions of images, our research indicates that the values of FD keep steady in breast phantoms with different CBTs and glandularity, and are lower than those of clinical images.

Admittedly, several limitations in this study need to be acknowledged. Firstly, the simulation of X-rays interaction was not involved in the ray tracing algorithm. In a follow-up study, Monte Carlo codes will be utilized to simulate the X-ray scattering and detector noise in the imaging geometry. The influence on the texture realism between simulated and clinical images may also come from various types of patient motions, including breathing, heartbeat, or compressed tissue relaxation. The negative effect of motions might be more pronounced in DBT acquisitions than in mammography due to the longer acquisition time and possible artifacts from reconstruction algorithms (Badal et al., 2021). In addition, only 1 commercial system was simulated in this study, and image processing algorithms and resolution may also affect the texture of simulated images. Secondly, further improvements can also be made to refine micro-structure in breast phantoms, including Cooper's ligament, adipose ellipsoid in the fibroglandular region, blood vessel network, and the boundary between the fibroglandular region

and the adipose region. Currently, Cooper's ligament is approximated using an ellipsoidal shell with a long main axis. However, Cooper's ligaments are made up of sheets of connective tissue that perform far more complex structures (Erickson et al., 2016). The vascular system grows randomly within the breast like a tree and is similar to the ductal system. The main limitation at present is that the growth of the vascular system conflicts with the ductal system, resulting in its inability to grow intact. In addition, the adipose ellipsoid in the fibroglandular region, and the boundary between the fibroglandular region and adipose region are irregular but smooth. To mimic the real structure of adipose, we need to add appropriate high-frequency noise to its surface. Additional investigations will still be conducted to enhance the texture realism of the detailed breast phantoms and the simulated images. Several studies have attempted to produce images comparable to clinical images, but they probably are not successful in the visualization test for clinical realism (Glick and Ikejimba, 2018). Plenty of ongoing efforts by VCTs researchers into breast phantom generation are still focusing on the improvement of texture realism (Barufaldi et al., 2021a). However, there remains a critical issue to be addressed a uniform standard for breast texture realism lacks. More investigations are needed to better understand this question.

Overall, we constructed two virtual imaging systems for DM and DBT, and validated that the breast phantom reflecting Chinese female anatomical characteristics performed well in both dosimetry and imaging. The breast phantoms used in this study employed a novel construction method. It contains most of the detailed structures present in the breast. Meanwhile, the irregular boundary between the skin region and the fibroglandular region, as well as the uneven distribution of adipose within the fibroglandular region, resulted in the inclusion of major breast textures in the imaging results. We have demonstrated the potential of this approach to provide valuable insights into device performance. Further research is still needed to address some of the limitations identified in our study, but our results lay a solid foundation for future work in this field.

An important implication of our work is to assess the radiation risks versus diagnosis benefits of breast cancer screening. In the field of breast X-ray imaging, the practical significance of this work will be better understood through a series of feasibility studies. Recently, the utilization of additive manufacturing and 3D printing techniques has emerged as a novel method for constructing phantoms in the field of medical physics, as well as for conducting research in x-ray breast imaging (Bliznakova, 2020). A number of researchers have conducted assessments on specimens composed of various materials, measuring attenuation coefficients within photon energy ranges typically employed in 2D and 3D x-ray mammography (Mettivier et al., 2022a; Santos et al., 2019; Savi et al., 2021). Based on the virtual breast phantoms, physically detailed breast phantoms can also be fabricated to replace homogeneous or heterogeneous breast models employed in experiments for quality control. In the field of breast dosimetry, the heterogeneous distribution of glandular in the detailed breast phantom allows for more individualized dose estimation for the patients. How to balance the radiation dose and image quality will be a vital direction of subsequent research in medical imaging.

#### 5. Conclusion

The breast imaging system is an essential part of VCTs. To the best of our knowledge, this work was undertaken to construct the breast phantom and the imaging system of both DM and DBT for the Chinese female population for the first time. A series of projections and reconstructed volumes were obtained from the detailed breast phantoms with different glandularity and CBTs for specific target/filter combinations and X-ray tube voltage. To evaluate the texture realism of simulated images, power spectrum analysis, and fractal dimension technique were employed for the analysis of the DM projections and DBT reconstructed mid-planes, and we obtained the values of power law exponents and

fractal dimensions for the simulated images. Compared to the clinical image datasets, the average power law exponent (clinical, simulated) for DM and DBT images were (3.26  $\pm$  0.29, 3.63  $\pm$  0.25) and (3.33  $\pm$  0.42, 3.18  $\pm$ 0.36) respectively. The average fractal dimension (clinical, simulated) for DM and DBT images were (2.36  $\pm$  0.03, 2.10  $\pm$  0.01) and (2.41  $\pm$  0.05, 2.26  $\pm$  0.06) respectively. For simulated and clinical images in DM and DBT, the values of power law exponents are positively correlated with the value of breast glandularity, but the values of fractal dimensions keep steady for different glandularity. These results indicate that the texture indexes of simulated images are similar to the clinical images. This work brings an important contribution to the image generation of VCTs with the detailed breast phantom. However, it still has certain limitations in terms of breast structure. In addition, another aspect to explore in the future is the design of more realistic glandular distributions and more complex surface texture of the microstructures.

#### Author statement

Jiahao Wang: Conceptualization, Methodology, Validation, Formal analysis, Investigation, Writing - Original Draft, Visualization, Data Curation.

Yeqi Liu: Investigation, Writing - Review & Editing.

Ankang Hu: Investigation, Writing - Review & Editing.

Shuoyang Wei: Writing - Review & Editing.

Tao Wu: Writing - Review & Editing.

Junli Li: Project administration, Funding acquisition.

Rui Qiu: Resources, Writing - Review & Editing, Project administration, Funding acquisition.

#### Declaration of competing interest

No potential conflict of interest was reported by the authors.

## Data availability

Data will be made available on request.

## Acknowledge:

This work was supported by the National Natural Science Foundation of China [Grant No. U2167209 and 12175114], the National Key R&D Program of China [Grant No. 2021YFF0603600], and Tsinghua University Initiative Scientific Research Program [Grant No. 20211080081]. We thank Dr. Tianliang Kang, An radiologist from Beijing Tongren Hospital, Captial Medical University, for his assistance in glandularity classification and texture realism evaluation.

## References

- Abadi, E., Segars, W.P., Tsui, B.M.W., Kinahan, P.E., Bottenus, N., Frangi, A.F., Maidment, A., Lo, J., Samei, E., 2020. Virtual clinical trials in medical imaging: a review. J. Med. Imag. 7.
- Badal, A., Sharma, D., Graff, C.G., Zeng, R.P., Badano, A., 2021. Mammography and breast tomosynthesis simulator for virtual clinical trials. Comput. Phys. Commun. 261.
- Bakic, P.R., Albert, M., Brzakovic, D., Maidment, A.D.A., 2002a. Mammogram synthesis using a 3D simulation. 1. Breast tissue model and image acquisition simulation. Med. Phys. 29, 2131–2139.
- Bakic, P.R., Albert, M., Brzakovic, D., Maidment, A.D.A., 2002b. Mammogram synthesis using a 3D simulation. II. Evaluation of synthetic mammogram texture. Med. Phys. 29, 2140–2151.
- Bakic, P.R., Albert, M., Brzakovic, D., Maidment, A.D.A., 2003. Mammogram synthesis using a three-dimensional simulation. III. Modeling and evaluation of the breast ductal network. Med. Phys. 30, 1914–1925.
- Bakic, P.R., Ng, S., Ringer, P., Carton, A.K., Conant, E.F., Maidment, A.D.A., 2010.
  Validation and Optimization of Digital Breast Tomosynthesis Reconstruction Using an Anthropomorphic Software Breast Phantom, Conference on Medical Imaging.
  Physics of Medical Imaging, San Diego, CA.
- Barufaldi, B., Higginbotham, D., Bakic, P.R., Maidment, A.D.A., 2018. OpenVCT: A GPU-Accelerated Virtual Clinical Trial Pipeline for Mammography and Digital Breast

- Tomosynthesis, Conference on Medical Imaging. Physics of Medical Imaging, Houston, TX.
- Barufaldi, B., Abbey, C.K., Lago, M.A., Vent, T.L., Acciavatti, R.J., Bakic, P.R., Maidment, A.D.A., 2021a. Computational breast anatomy simulation using multiscale Perlin noise. IEEE Trans. Med. Imag. 40, 3436–3445.
- Barufaldi, B., Maidment, A.D.A., Dustler, M., Axelsson, R., Tomic, H., Zackrisson, S., Tingberg, A., Bakic, P.R., 2021b. Virtual clinical trials in medical imaging system evaluation and optimisation. Radiat. Protect. Dosim. 195, 363–371.
- Bliznakova, K., Bliznakov, Z., Bravou, V., Kolitsi, Z., Pallikarakis, N., 2003. A threedimensional breast software phantom for mammography simulation. Phys. Med. Biol. 48, 3699–3719.
- Bliznakova, K., Suryanarayanan, S., Karellas, A., Pallikarakis, N., 2010. Evaluation of an improved algorithm for producing realistic 3D breast software phantoms: application for mammography. Med. Phys. 37, 5604–5617.
- Bliznakova, K., 2020. The advent of anthropomorphic three-dimensional breast phantoms for X-ray imaging. Phys. Med. 79, 145–161.
- Bochud, F.O., Abbey, C.K., Eckstein, M.P., 1999. Statistical texture synthesis of mammographic images with clustered lumpy backgrounds. Opt Express 4, 33–43.
- Boone, J.M., Fewell, T.R., Jennings, R.J., 1997. Molybdenum, rhodium, and tungsten anode spectral models using interpolating polynomials with application to mammography. Med. Phys. 24, 1863–1874.
- Buda, M., Saha, A., Walsh, R., Ghate, S., Li, N., Swiecicki, A., Lo, J.Y., Mazurowski, M.A., 2021. A data set and deep learning algorithm for the detection of masses and architectural distortions in digital breast tomosynthesis images. JAMA Netw. Open 4.
- Burgess, A.E., Jacobson, F.L., Judy, P.F., 2001. Human observer detection experiments with mammograms and power-law noise. Med. Phys. 28, 419–437.
- Caballo, M., Rabin, C., Fedon, C., Rodriguez-Ruiz, A., Diaz, O., Boone, J.M., Dance, D.R., Sechopoulos, I., 2022. Patient-derived heterogeneous breast phantoms for advanced dosimetry in mammography and tomosynthesis. Med. Phys. 49, 5423–5438.
- Cao, W., Chen, H.D., Yu, Y.W., Li, N., Chen, W.Q., 2021. Changing profiles of cancer burden worldwide and in China: a secondary analysis of the global cancer statistics 2020. Chinese Med J 134, 783–791.
- Cockmartin, L., Bosmans, H., Marshall, N.W., 2013. Comparative power law analysis of structured breast phantom and patient images in digital mammography and breast tomosynthesis. Med. Phys. 40.
- Elangovan, P., Mackenzie, A., Dance, D.R., Young, K.C., Cooke, V., Wilkinson, L., Given-Wilson, R.M., Wallis, M.G., Wells, K., 2017. Design and validation of realistic breast models for use in multiple alternative forced choice virtual clinical trials. Phys. Med. Biol. 62, 2778–2794.
- Erickson, D.W., Wells, J.R., Sturgeon, G.M., Samei, E., Dobbins, J.T., Segars, W.P., Lo, J. Y., 2016. Population of 224 realistic human subject-based computational breast phantoms. Med. Phys. 43, 23–32.
- Glick, S.J., Ikejimba, L.C., 2018. Advances in digital and physical anthropomorphic breast phantoms for x-ray imaging. Med. Phys. 45, e870–e885.
- Gorshkov, V., 2017. The effective atomic number and the mass attenuation coefficient of a multicomponent object for the continuous spectrum of the radiation. Nondestr. Test. Eval. 32, 79–89.
- Graff, C.G., 2016. A New, Open-Source, Multi-Modality Digital Breast Phantom, Conference on Medical Imaging. Physics of Medical Imaging, San Diego, CA
- Heine, J.J., Velthuizen, R.P., 2000. A statistical methodology for mammographic density detection. Med. Phys. 27, 2644–2651.
- Helvie, M.A., Chang, J.T., Hendrick, R.E., Banerjee, M., 2014. Reduction in late-stage breast cancer incidence in the mammography era. Cancer 120, 2649–2656.
- Hsu, C.M.L., Palmeri, M.L., Segars, W.P., Veress, A.I., Dobbins III, J.T., 2013. Generation of a suite of 3D computer-generated breast phantoms from a limited set of human subject data. Med. Phys. 40.
- Hubbell, J.H., Seltzer, S.M., 2004. NIST standard reference Database 126. https://www.nist.gov/pml/x-ray-mass-attenuation-coefficients.
- Ikejimba, L.C., Graff, C.G., Rosenthal, S., Badal, A., Ghammraoui, B., Lo, J.Y., Glick, S.J., 2017. A novel physical anthropomorphic breast phantom for 2D and 3D x-ray imaging. Med. Phys. 44, 407–416.
- Kwan, A.L.C., Boone, J.M., Yang, K., Huang, S.-Y., 2007. Evaluation of the spatial resolution characteristics of a cone-beam breast CT scanner. Med. Phys. 34, 275–281
- Lau, B.A., Reiser, I., Nishikawa, R.M., Bakic, P.R., 2012. A statistically defined anthropomorphic software breast phantom. Med. Phys. 39, 3375–3385.
- Li, C.M., Segars, W.P., Tourassi, G.D., Boone, J.M., Dobbins III, J.T., 2009. Methodology for generating a 3D computerized breast phantom from empirical data. Med. Phys. 36, 3122–3131.
- Ma, A.K.W., Gunn, S., Darambara, D.G., 2009. Introducing DeBRa: a detailed breast model for radiological studies. Phys. Med. Biol. 54, 4533–4545.
- Mahr, D.M., Bhargava, R., Insana, M.F., 2012. Three-dimensional in silico breast phantoms for multimodal image simulations. IEEE Trans. Med. Imag. 31, 689–697.
- Mainprize, J.G., Tyson, A.H., Yaffe, M.J., 2012. The relationship between anatomic noise and volumetric breast density for digital mammography. Med. Phys. 39, 4660–4668.
- Marinov, S., Buliev, I., Cockmartin, L., Bosmans, H., Bliznakov, Z., Mettivier, G., Russo, P., Bliznakova, K., 2021. Radiomics software for breast imaging optimization and simulation studies. Physica Medica-European Journal of Medical Physics 89, 114–128.
- Marshall, N.W., Bosmans, H., 2022. Performance evaluation of digital breast tomosynthesis systems: comparison of current virtual clinical trial methods. Phys. Med. Biol. 67.
- Massera, R.T., Tomal, A., 2021. Breast glandularity and mean glandular dose assessment using a deep learning framework: virtual patients study. Phys. Med. 83, 264–277.

- Mettivier, G., Sarno, A., Varallo, A., Russo, P., 2022a. Attenuation coefficient in the energy range 14-36 keV of 3D printing materials for physical breast phantoms. Phys. Med. Biol. 67.
- Mettivier, G., Sarno, A., Lai, Y.F., Golosio, B., Fanti, V., Italiano, M.E., Jia, X., Russo, P., 2022b. Virtual clinical trials in 2D and 3D X-ray breast imaging and dosimetry: comparison of CPU-based and GPU-based Monte Carlo codes. Cancers 14.
- National Health Commission, 2020. Specification for Testing of Quality Control in Medical X-Ray Diagnostic Equipment. http://www.nhc.gov.cn/wjw/pcrb/202101/1 478bfbdcaf0423e93dd17caf5f1e798.shtml.
- National Health Commission, 2021. Methods for Estimation of Examinee's Organ Doses in X-Ray Diagnosis. https://openstd.samr.gov.cn/bzgk/gb/newGbInfo?hcno=854 EBAC6FF951F325F2B0D3AFD7DC04F.
- Pertuz, S., Torres, G.F., Tamimi, R., Kamarainen, J., Ieee, 2019. Open Framework for Mammography-Based Breast Cancer Risk Assessment, IEEE EMBS International Conference on Biomedical and Health Informatics (BHI). Univ Illinois Chicago, Chicago, IL.
- Pokrajac, D.D., Maidment, A.D.A., Bakic, P.R., 2012. Optimized generation of high resolution breast anthropomorphic software phantoms. Med. Phys. 39, 2290–2302.
- Qiu, R., Jiang, C., Ren, L., Li, C., Wu, Z., Li, J., 2017. Establishment of the detailed breast model of Chinese adult female and application in external radiation protection. Radiat. Protect. Dosim. 174, 113–120.
- Santos, J.C., Almeida, C.D., Iwahara, A., Peixoto, J.E., 2019. Characterization and applicability of low-density materials for making 3D physical anthropomorphic breast phantoms. Radiat. Phys. Chem. 164.
- Sarno, A., Dance, D.R., van Engen, R.E., Young, K.C., Russo, P., Di Lillo, F., Mettivier, G., Bliznakova, K., Fei, B.W., Sechopoulos, I., 2017a. A Monte Carlo model for mean glandular dose evaluation in spot compression mammography. Med. Phys. 44, 3848–3860.
- Sarno, A., Mettivier, G., Di Lillo, F., Russo, P., 2017b. A Monte Carlo study of monoenergetic and polyenergetic normalized glandular dose (DgN) coefficients in mammography. Phys. Med. Biol. 62, 306–325.
- Sarno, A., Mettivier, G., Di Lillo, F., Bliznakova, K., Sechopoulos, I., Russo, P., 2018a. Homogeneous vs. patient specific breast models for Monte Carlo evaluation of mean glandular dose in mammography. Phys. Med. 51, 56–63.
- Sarno, A., Mettivier, G., Tucciariello, R.M., Bliznakova, K., Boone, J.M., Sechopoulos, I., Di Lillo, F., Russo, P., 2018b. Monte Carlo evaluation of glandular dose in cone-beam X-ray computed tomography dedicated to the breast: homogeneous and heterogeneous breast models. Phys. Med. 51, 99–107.
- Sarno, A., Mettivier, G., di Franco, F., Patern, G., Taibi, A., Cardarelli, P., Tucciariello, R.
   M., Kristina, M.E., Bliznakova, K., Hernandez, A.H., Boone, J.M., Russo, P., 2020.
   Advanced Monte Carlo Application for in Silico Clinical Trials in X-Ray Breast Imaging, 15th International Workshop on Breast Imaging (IWBI). Electr Network.
- Sarno, A., Tucciariello, R.M., Mettivier, G., Del Sarto, D., Fantacci, M.E., Russo, P., 2021. Normalized glandular dose coefficients for digital breast tomosynthesis systems with a homogeneous breast model. Phys. Med. Biol. 66.
- Sarno, A., Mettivier, G., Bliznakova, K., Hernandez, A.M., Boone, J.M., Russo, P., 2022.
  Comparisons of glandular breast dose between digital mammography, tomosynthesis

- and breast CT based on anthropomorphic patient-derived breast phantoms. Phys. Med. 97, 50–58.
- Sarno, A., Valero, C., Tucciariello, R.M., Dukov, N., Costa, P.R., Tomal, A., 2023. Physical and digital phantoms for 2D and 3D x-ray breast imaging: review on the state-of-the-art and future prospects. Radiat. Phys. Chem. 204.
- Savi, M., Villani, D., Andrade, M.A.B., Rodrigues, O., Potiens, M.P.A., 2021. Study on attenuation of 3D printing commercial filaments on standard X-ray beams for dosimetry and tissue equivalence. Radiat. Phys. Chem. 182.
- Sturgeon, G.M., Park, S., Segars, W.P., Lo, J.Y., 2017. Synthetic breast phantoms from patient based eigenbreasts. Med. Phys. 44, 6270–6279.
- Suckling, J., Boggis, C.R.M., Hutt, I., Astley, S., Betal, D., Cerneaz, N., Dance, D.R., Kok, S.L., Parker, J., Ricketts, I., Savage, J., Stamatakis, E., Taylor, P., 2015. The Mammographic Image Analysis Society Digital Mammographic Database. Figshare.
- Tagliafico, A., Mariscotti, G., Durando, M., Stevanin, C., Tagliafico, G., Martino, L., Bignotti, B., Calabrese, M., Houssami, N., 2015. Characterisation of microcalcification clusters on 2D digital mammography (FFDM) and digital breast tomosynthesis (DBT): does DBT underestimate microcalcification clusters? Results of a multicentre study. Eur. Radiol. 25, 9–14.
- Tourassi, G.D., Delong, D.M., Floyd, C.E., 2006. A study on the computerized fractal analysis of architectural distortion in screening mammograms. Phys. Med. Biol. 51, 1299–1312.
- Vancamberg, L., Carton, A.K., Abderrahmane, I.H., Palma, G., de Carvalho, P.M., Iordache, R., Muller, S., 2015. Influence of DBT Reconstruction Algorithm on Power Law Spectrum Coefficient, Conference on Medical Imaging. Physics of Medical Imaging, Orlando, FL.
- Vimieiro, R.B., Borges, L.R., Vieira, M.A.C., 2018. Open-Source Reconstruction Toolbox for Digital Breast Tomosynthesis, 26th Brazilian Congress on Biomedical Engineering (CBEB). Armacao de Buzios, BRAZIL, pp. 349–354.
- Wang, M.R., Zhuang, S., Sheng, L.L., Zhao, Y.N., Shen, W.R., 2022. Performance of full-field digital mammography versus digital breast. Precision Medical Sciences 11, 56–61.
- Wang, W.J., Qiu, R., Ren, L., Liu, H., Wu, Z., Li, C.Y., Niu, Y.T., Li, J.L., 2017. Monte Carlo calculation of conversion coefficients for dose estimation in mammography based on a 3D detailed breast model. Med. Phys. 44, 2503–2514.
- Woodard, H.Q., White, D.R., 1986. The composition of body-tissues. Br. J. Radiol. 59, 1209–1219
- Wu, T., Stewart, A., Stanton, M., McCauley, T., Phillips, W., Kopans, D.B., Moore, R.H., Eberhard, J.W., Opsahl-Ong, B., Niklason, L., Williams, M.B., 2003. Tomographic mammography using a limited number of low-dose cone-beam projection images. Med. Phys. 30, 365–380.
- Zeng, R.P., Park, S., Bakic, P., Myers, K.J., 2015. Evaluating the sensitivity of the optimization of acquisition geometry to the choice of reconstruction algorithm in digital breast tomosynthesis through a simulation study. Phys. Med. Biol. 60, 1259–1288.
- Zyganitidis, C., Bliznakova, K., Pallikarakis, N., 2007. A novel simulation algorithm for soft tissue compression. Med. Biol. Eng. Comput. 45, 661–669.